High-Resolution Simulation and Analysis of the Mature Structure of a Polar Low over the Sea of Japan on 21 January 1997

FU Gang*[1,2,3] (傅 刚), GUO Jingtian[1] (郭敬天), and ZHANG Meigen[3] (张美根)

[1] *Department of Marine Meteorology, Ocean University of China, Qingdao* 266003

[2] *Laboratory of Physical Oceanography, Ocean University of China, Qingdao* 266003

[3] *State Key Laboratory of Atmospheric Boundary Layer Physics and Atmospheric Chemistry, Institute of Atmospheric Physics, Chinese Academy of Sciences, Beijing* 100029

(Received 18 August 2003; revised 12 December 2003)

ABSTRACT

This paper presents a high-resolution simulation of a remarkable polar low observed over the Sea of Japan on 21 January 1997 by using a 5-km mesh non-hydrostatic model MRI-NHM (Meteorological Research Institute Non-Hydrostatic Model). A 24-hour simulation starting from 0000 UTC 21 January 1997 successfully reproduced the observed features of the polar low such as the wrapping of western part of an initial E–W orientation vortex, the spiral-shaped bands, the cloud-free "eye", and the warm core structure at its mature stage. The "eye" of the simulated polar low was relatively dry, and was associated with a strong downdraft. A thermodynamic budget analysis indicates that the "warm core" in the "eye" region was mainly caused by the adiabatic warming associated with the downdraft. The relationship among the condensational diabatic heating, the vertical velocity, the convergence of the moisture flux, and the circulation averaged within a 50 km×50 km square area around the polar low center shows that they form a positive feedback loop, and this loop is not inconsistent with the CISK (Conditional Instability of the Second Kind) mechanism during the developing stage of the polar low.

Key words: polar low, Sea of Japan, high-resolution simulation, warm core structure

1. Introduction

Polar lows (Harley, 1960) are intense meso-scale cyclones that form in cold air streams of the polar air mass in winter. Their horizontal scales are on the order of several hundred kilometers, and their lifetimes range from several hours to several days. They usually develop over high-latitude oceans in winter such as the Gulf of Alaska (50°–60°N, 135°–160°W), the Barents Sea (65°–75°N, 20°–50°E), the Labrador Sea (55°–65°N, 50°–60°W), and the Norwegian Sea (60°–70°N, 5°–10°E). On satellite images, polar lows are frequently characterized by spiral- or comma-shaped cloud patterns and are even associated with a clear "eye" structure at the mature stage. As polar lows often cause severe weather such as strong wind and heavy snowfall, they are thought to be one of the most dangerous weather systems.

In the past decades, polar lows have received considerable attention in the literature (Mansfield, 1974; Rasmussen, 1979; Shapiro et al., 1987; Ninomiya, 1989; Tsuboki and Wakahama, 1992; Lee et al., 1998; Fu, 1999; Fu, 2001; Yanase et al., 2002; Fu et al., 2004). Among the oceans where polar lows frequently occur, the Sea of Japan is located in the lowest latitude position. Moreover, since the Sea of Japan is almost surrounded by the Eurasian Continent and the Japan Islands, it is thought to be one of the most suitable areas to study polar lows: in the upstream of the Sea of Japan, a great number of upper air observation stations are spread over the continent; in the downstream, when polar lows make landfall on the Japan Islands, more detailed observational data can be obtained from the radar networks and AMeDAS (Automated Meteorological Data Acquisition System).

During 20–21 January 1997, a remarkable polar low occurred over the Sea of Japan. Using almost all available observational data including the GMS-5 (Geosta-

*E-mail: fugang@ouc.edu.cn

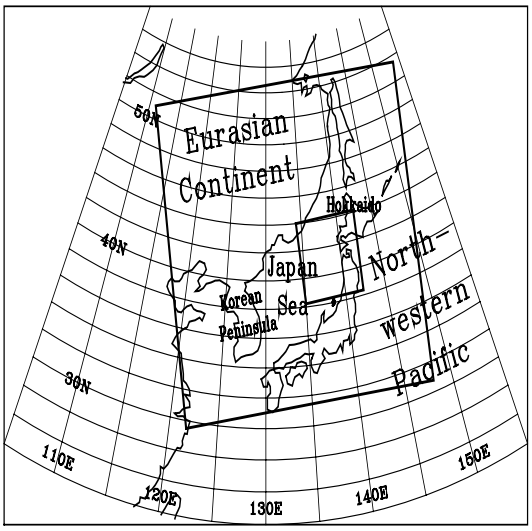

Fig. 1. Geographic map for East Asia and the Northwestern Pacific. The large square shows the calculation domain of the RSM simulation that provides the initial and boundary conditions for the MRI-NHM simulation, while the small square is the domain for the MRI-NHM simulation.

tionary Meteorological Satellite) TBB (blackbody temperature) data as well as Sapporo and Niigata radar data, Fu (1999) documented the detailed evolutionary process of this polar low event and the environmental conditions that led to its generation. When the polar low was at its mature stage, a typical spiral-shaped cloud pattern and a clear "eye" structure was observed from the satellite and radar images. Also, a warm core structure associated with the polar low was found at lower levels. The mechanisms for the spiral-shaped cloud pattern and clear "eye" structure are an interesting topic and warrant further investigations.

Although Yanase et al. (2002) performed a numerical simulation of this polar low case, its development mechanism has not been revealed yet. In this paper, a 5-km mesh numerical simulation of this polar low case using MRI-NHM (Meteorological Research Institute Non-Hydrostatic Model) is conducted to examine its detailed characteristics at the mature stage and its development mechanism. The paper is organized as follows. In section 2, the numerical model MRI-NHM used in the present study is introduced. In section 3, the detailed mature structure of the polar low is examined based upon the simulation results of MRI-NHM. Finally in section 4, discussion and conclusion are given.

2. Description of MRI-NHM

MRI-NHM is a three-dimensional non-hydrostatic model developed by the Forecast Research Department of the Meteorological Research Institute, Japan (Ikawa and Saito, 1991; Saito and Kato, 1996), and modified so that it can be nested within an outer coarse-mesh model (Saito, 1994). The main features of MRI-NHM are summarized in Table 1.

Table 1. Specification of the MRI-NHM.

Categories	Specification in the present study
Baisc equations	Fully compressible non-hydrostatic Navirer-stokes equations with a map factor (Saito, 1997)
Vertical coordinate	Terrain-following (Gal-chen and Somerville, 1975) 38 levels (fine resolution in the boundary layer)
Projection	North polar stereographic projection
Advection scheme	Arakawa-c grid (lkawa and Saito, 1991) second order flux form Box-Lagrangian raindrop scheme (Kato, 1995)
Horizontal resolution	5-km (at 32.5°N)
Time integration	Both vertically and horizontally implicit for sound waves (Δt =10 s)
Turbulent closure	Deardorff level 2.5 (Saito, 1993)
Precipitation scheme	Cold rain scheme (predicting $q_{\rm v}, q_{\rm c}, q_{\rm r}, q_{\rm i}, q_{\rm s}, q_{\rm g}$)
Radiation	Long and shortwave radiation
Surface processes	Surface heat balance (Sommeria, 1976; Kondo, 1975)
Lower boundary	Forecast using 4-layer model (Kato, 1996)
Upper boundary	Rigid lid, thermally insulated Rayleigh friction layer
Lateral boundary	Radiative nesting boundary condition (Saito, 1994). Nesting within RSM (Saito, 1998)
Numerical diffusion	4-th order linear damping
Initial time	0000 UTC 21 January 1997
Integration period	24 h

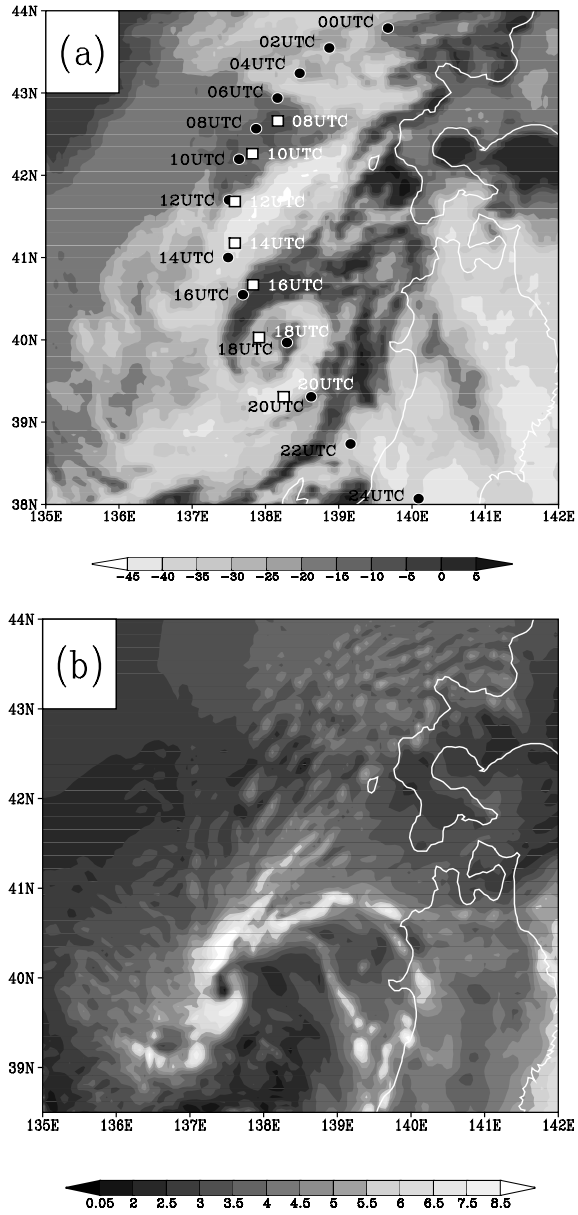

Fig. 2. (a) GMS-5 TBB image at 1800 UTC January 1997. The polar low was at its mature stage. The movement of the observed polar low is indicated by black circles every 2-h from 0000 to 2400 UTC, and that of the simulated one by white rectangles from 0800 to 2000 UTC with a 2-h interval (the units of the color bar are °C). (b) Vertically integrated total water at 1800 UTC January 1997 based upon MRI-NHM simulation results (the units of the color bar are kg m^{-2}).

The model using a vertical terrain-following coordinate is formulated in terms of the fully compressible Navier-Stokes equations with a map factor. In the model, a box-Lagrangian rain-drop scheme (Kato, 1995) is employed, and the ground temperature is predicted (Kato, 1996). A cold rain scheme is used in which the six variables of mixing ratios of water vapor q_v, cloud q_c, rain q_r, ice q_i, snow q_s and graupel q_g are predicted.

In the present study, the calculation domain was chosen to cover the path of the polar low center at its initial and developing stages (small domain in Fig. 1). It has 122×122 horizontal grid points. The horizontal grid sizes are Δx=Δy=5 km. The number of vertical grid points is 38, where the grid interval is smaller near the surface*. The model top is located at 20.36 km. The time step of integration Δt is 10 s. The initial and boundary conditions are taken from the 24-h prediction of RSM (Regional Spectral Model), a primitive equation model for operational numerical prediction of the Japan Meteorological Agency (Nakamura, 1995) starting from 0000 UTC 21 January 1997. The horizontal resolution of RSM is Δx=Δy= 20 km (large domain in Fig. 1). During the MRI-NHM model run, the SST field is fixed with interpolating 1° × 1° SST data at 1200 UTC 21 January 1997. The initial time of the MRI-NHM simulation is 0000 UTC 11 January 1997 and the model integration time is 24 h**.

3. Results

3.1 *Model verification*

Figure 2a presents the two-hourly positions of the polar low observed by GMS-5 imagery together with the simulated polar low whose centers have been determined from the surface pressure minimum. Figure 2b shows the horizontal distribution of vertically integrated total water (i.e., sum of the vertical integration of water vapor, cloud water, ice, rain, snow, and graupel) at 1800 UTC 21 January 1997, when the polar low was at its mature stage. The simulated features of a cloud-free "eye" with two major spiral bands extending from the low center to north and west respectively, and the cloud streets on the northern and western side of the spiral bands are similar to those observed by GMS-5 (see Fig. 2a). It is believed that MRI-NHM reproduced the movement of the polar low fairly satisfactorily, although a few discrepancies exist between the observations and simulations. Generally, this is a successful simulation of a polar low over the Sea of Japan with a high-resolution non-hydrostatic model.

*The level heights are 0.02, 0.06, 0.13, 0.23, 0.36, 0.52, 0.71, 0.93, 1.18, 1.46, 1.77, 2.11, 2.48, 2.88, 3.31. 3.77, 4.26, 4.78, 5.33, 5.91, 6.52, 7.16, 7.83, 8.53, 9.26, 10.02, 10.81, 11.63, 12.48, 13.36, 14.27, 15.21, 16.18, 17.18, 18.21, 19.27, and 20.36 km, respectively.

**Due to the limitation of our computer resources, the calculation domain of MRI-NHM has to be kept small. Accordingly, the polar low moved southward and went out of the domain after 2200 UTC.

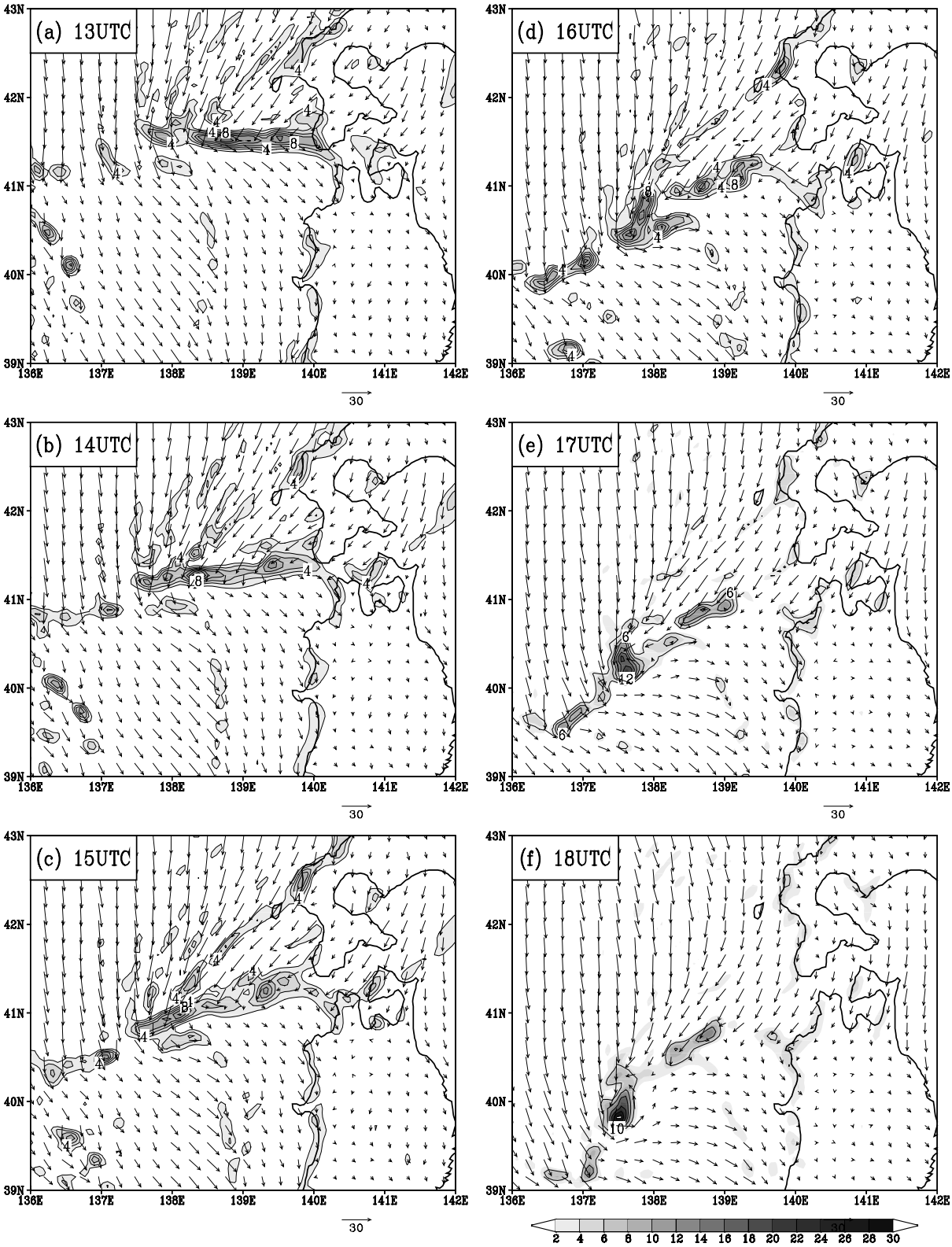

Fig. 3. The wind vector and vorticity field (in 10^{-4} s^{-1}) from 1300 to 1800 UTC 21 January 1997 simulated by MRI-NHM. The evolutionary process of the wrapping of the western part of the vorticity band can be seen clearly. (a) 1300 UTC, (b) 1400 UTC, (c) 1500 UTC, (d) 1600 UTC, (e) 1700 UTC, (f) 1800 UTC.

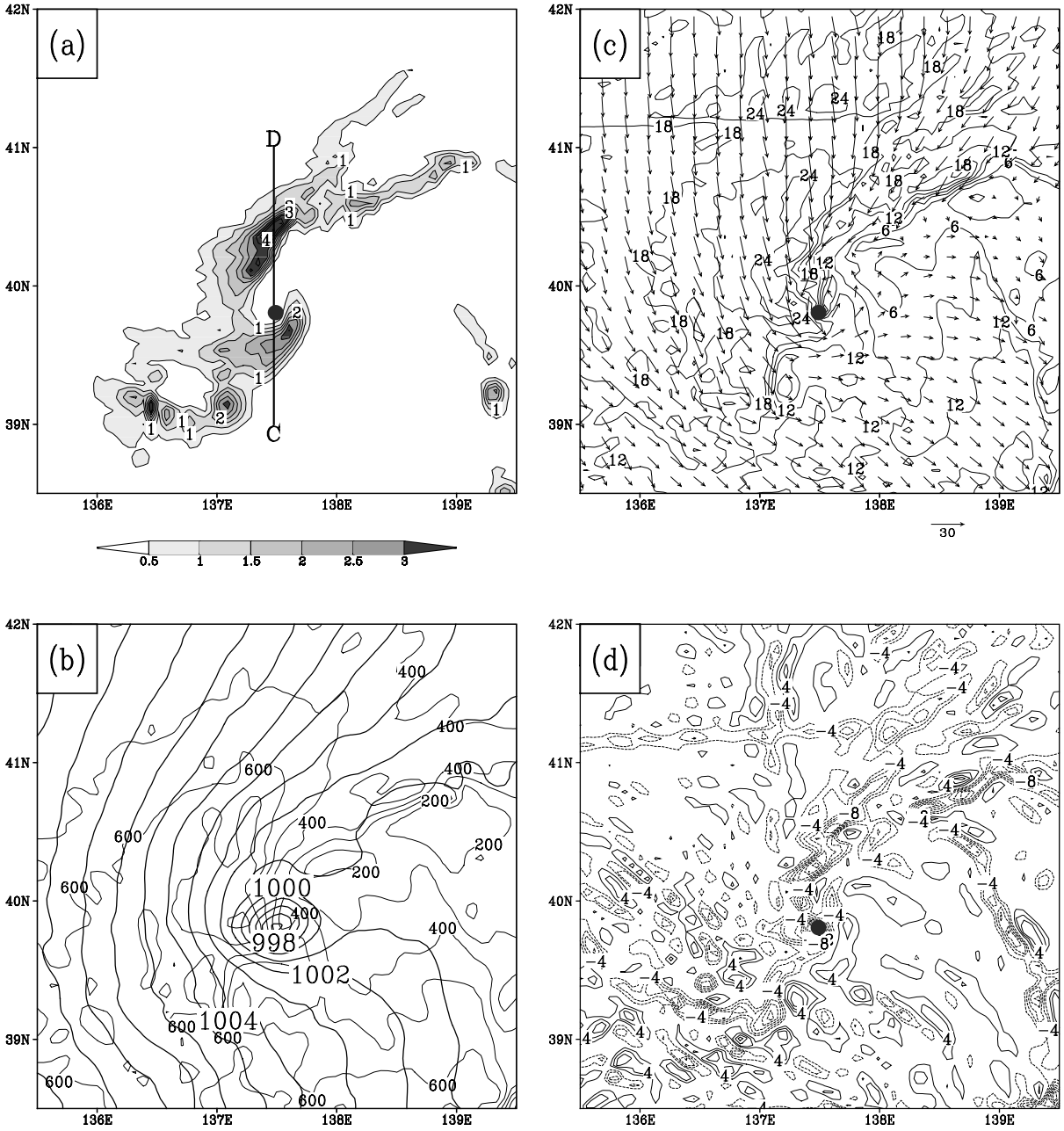

Fig. 4. At 1800 UTC 21 January 1997. (a) vertically integrated snow per unit area (kg m^{-2}). (b) surface pressure (thick line, in hPa) and total surface heat flux (thin line, in W m^{-2}). (c) surface wind vector and wind speed (m s^{-1}). (d) surface divergence (10^{-4} s^{-1}). The surface low center is indicated by a black dot.

The simulation results of MRI-NHM can also be verified from the view of the wrapping of the western part of an initial E–W oriented cloud band (Fu, 2001). Figure 3 shows the simulated vorticity field and wind vectors at the lowest model level (altitude of 20 m) from 1300 to 1800 UTC 21 January 1997. At 1300 UTC, an E–W oriented high vorticity region is clearly seen around the latitude line 41.5°N (Fig. 3a). This high vorticity region corresponds to a shear zone between the northeasterly wind to the north and the north-northwesterly wind to the south. Such a feature corresponds well to the observed structure of the E–W oriented cloud band except that the intensification ofthe polar low is somewhat delayed in the simulation (Fu, 2001). The maximum vorticity that seems to correspond to the initial polar low is located near (41.5°N, 138.8°E).

The evolutionary process of the wrapping of the

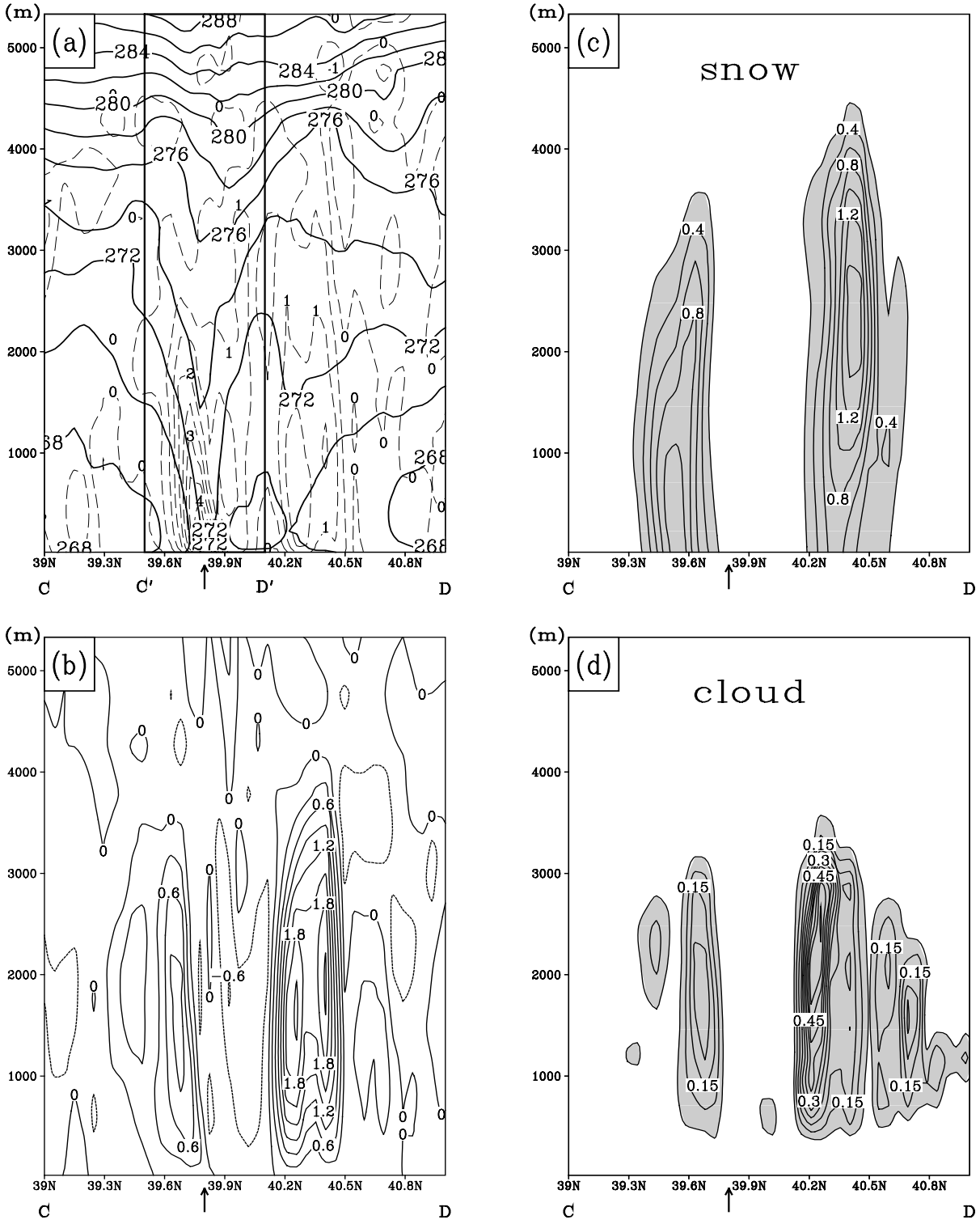

Fig. 5. Vertical cross-section analyses along the line CD as indicated in Fig. 4a. (a) potential temperature θ (solid line, in K) and vorticity (dashed line, in $10^{-3}\ \mathrm{s}^{-1}$). The frame labeled with C′ and D′ will be enlarged for detailed examination in Fig. 6, (b) vertical velocity w ($\mathrm{m\,s}^{-1}$), (c) snow mixing ratio q_s (in $10^{-3}\ \mathrm{kg\,kg}^{-1}$), (d) cloud mixing ratio q_c (in $10^{-3}\ \mathrm{kg\,kg}^{-1}$). The surface low center is indicated by an arrow.

western part of the vorticity band can be seen clearly from the series of the vorticity field. Figures 3b and c show that the principal axis of the high vorticity region started to rotate anti-clockwise. As the time elapsed, the high vorticity region gradually lost its approximate uniformity in the direction of the principal axis. It is also noted that the eastern part of the high vorticity region became weaker. The initial polar low moved southwestward while keeping its vorticity level. After 1600 UTC (Figs. 3d and e), the polar low changed its direction of movement to southward and started to develop rapidly. At 1800 UTC (Fig. 3f), the vortex attained its mature stage. The timing of the development of the polar low is somewhat late compared to the observation. Considering the small-scale vortices, however, the simulation seems to be quite satisfactory. Accordingly, we will examine the detailed structure of the mature polar low at 1800 UTC in the following.

3.2 *Structure of the simulated polar low*

Figure 4a shows the horizontal distribution of vertically integrated snow per unit area at 1800 UTC 21 January 1997*. The spiral-shaped cloud band extending northeastward from the low center and a clear "eye" structure surrounded by the spiral-shaped cloud are seen**.

Figure 4b shows the horizontal distributions of the total surface heat flux together with the surface pressure at 1800 UTC 21 January 1997. Generally speaking, the sensible heat flux is about 1.5 times as large as the latent heat flux. The total heat flux has a remarkable east-west asymmetry. In the western quadrant of the low, the total surface heat flux exceeds 800 W m^{-2}, while it is less than 300 W m^{-2} on the eastern side. This asymmetry in the total heat flux is mainly caused by the asymmetry of the wind speed. Figure 4c shows the horizontal wind vectors and the magnitude of the wind speed. It is seen that a strong northerly wind with a maximum wind speed of 24 m s^{-1} prevails on the northwestern side of the low, while on the eastern side, the magnitude of the wind speed is strikingly smaller than that of the western side. A strong convergence center is seen near the surface low center (Fig. 4d).

Figure 5 shows the vertical cross section of potential temperature and vorticity, vertical velocity, and mixing ratios of snow and cloud along the line CD as indicated in Fig. 4a. The surface polar low center identified by a pressure minimum is indicated by an arrow. In the "eye" area, a sharp lowering of the contour lines of potential temperature θ is found (Fig. 5a), showing a "warm core" structure. It is also seen that at this mature stage of the polar low, its vorticity is mostly concentrated below 2000 m, and is largest around 250 m above sea level (Fig. 5a). There are two regions of large vorticity on the northern and southern sides of the "eye" that are about 50 km apart. They correspond to the spiral cloud bands. The maximum vorticity on the southern side reaches 4.5×10^{-3} s^{-1}. The distribution of the vertical velocity w shows that the central part of the "eye" is associated with a significant downdraft with the maximum value of –0.6 m s^{-1}, while on the southern side of the "eye" an updraft with a maximum value of 0.9 m s^{-1} is found (Fig. 5b). The maximum updraft in the northern spiral band from 40.2°N to 40.4°N reaches 2.1 m s^{-1}. The distributions of the mixing ratios of snow q_s (Fig. 5c) and cloud q_c (Fig. 5d) show that the "eye" is almost free of snow and cloud.

3.3 *The thermodynamical analysis of the warm core in the eye*

In order to examine the "eye" structure in more detail, the region between C′ and D′ in Fig. 5a is enlarged. Figure 6a shows the vertical cross section of the mixing ratio of water vapor q_v and the potential temperature θ. The "eye" area at 500 m above sea level is about 3–4°C warmer than the environment, and it is also accompanied with a "dry core" around the height of 1500–3500 m with a minimum mixing ratio q_v of 0.2 kg kg^{-1}. In order to investigate how the "warm core" was formed, a thermodynamic budget analysis was performed. Figures 6b–d show the potential temperature θ together with the diabatic heating dQ/dt, the horizontal advection term $-\boldsymbol{V}_h\cdot\nabla\theta$, and the vertical advection term $-w\partial\theta/\partial z$, respectively. It is found that in the "eye" area, the contribution of diabatic heating dQ/dt is less than 1 K h^{-1} (Fig. 6b). The contribution of the horizontal advection $-\boldsymbol{V}_h\cdot\nabla\theta$ changes sign along the line connecting the maximum positive potential temperature anomaly (Fig. 6c), which indicates that the main contribution of this term is to shift the potential temperature pattern toward the moving direction of the polar low. It does not contribute to increase the potential temperature anomaly. Only the contribution of the vertical advection associated with the downdraft is positive and is larger than 1 K h^{-1}

*Here we only show the mixing ratio of snow q_s, since it is the largest among q_c, q_g, q_i, and q_r. The maximum values of the vertically integrated q_c, q_g, q_i, and q_r are 1.1, 0.9, 0.22, and 0.035 kg m^{-2}, respectively, which are considerably smaller than 4.6 for q_s

**Yanase et al. (2002) confirmed that a 2-km mesh MRI-NHM could reproduce the present polar low successfully. However, they did not report a detailed analysis of the present case

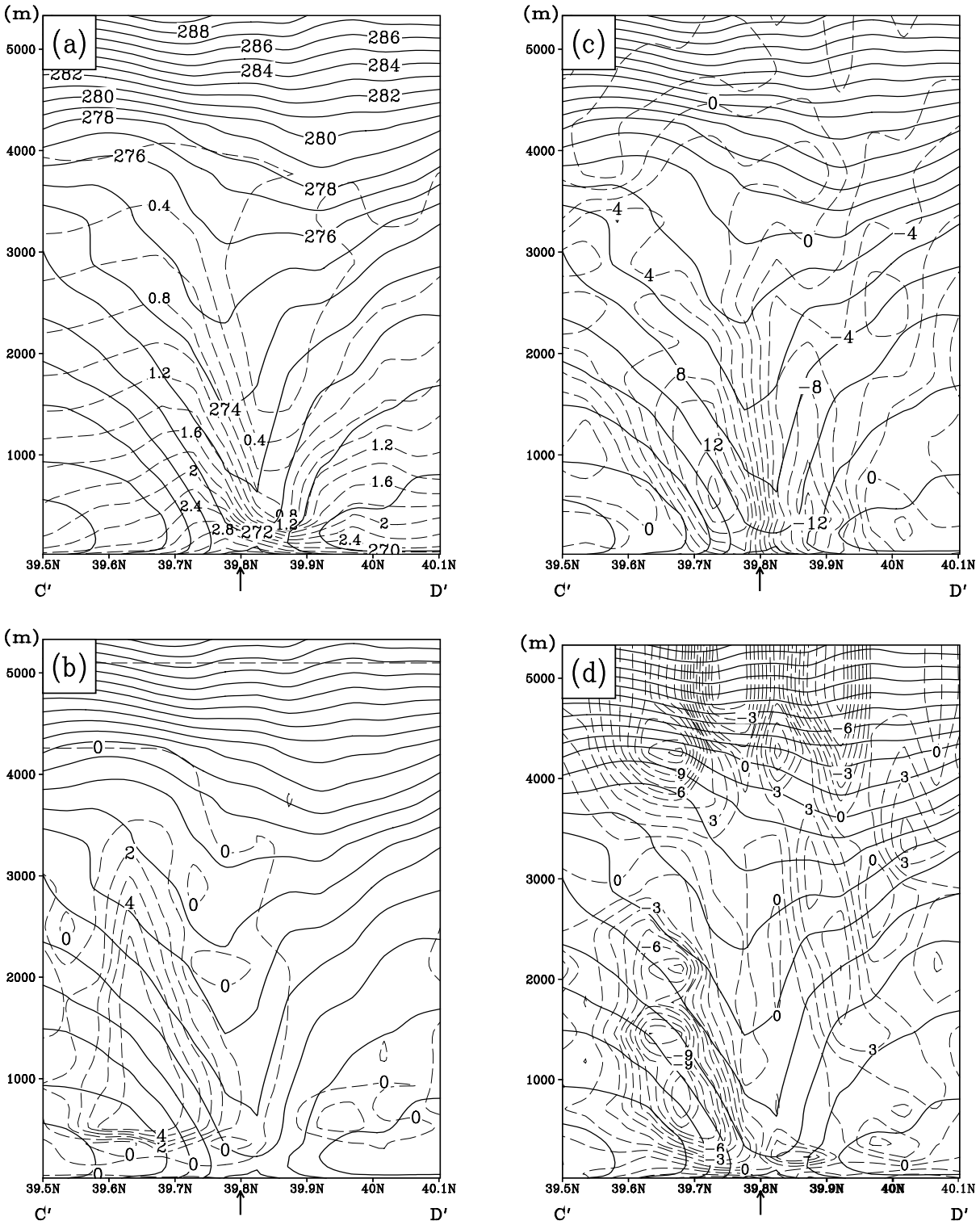

Fig. 6. Vertical cross-section analyses along the line C′D′. (a) potential temperature θ (solid line, in K) and mixing ratio of water vapor q_{v} (dashed line, in kg kg^{-1}), (b) θ (solid line, in K) and diabatic heating (dashed line, in K h^{-1}). (c) θ (solid line, in K) and horizontal advection $-\boldsymbol{V}_{\mathrm{h}} \cdot \nabla\theta$ (dashed line, in K h^{-1}). (d) θ (solid line, in K) and vertical advection $-w\partial\theta/\partial z$. (dashed line, in K h^{-1}). The surface low center is indicated by an arrow.

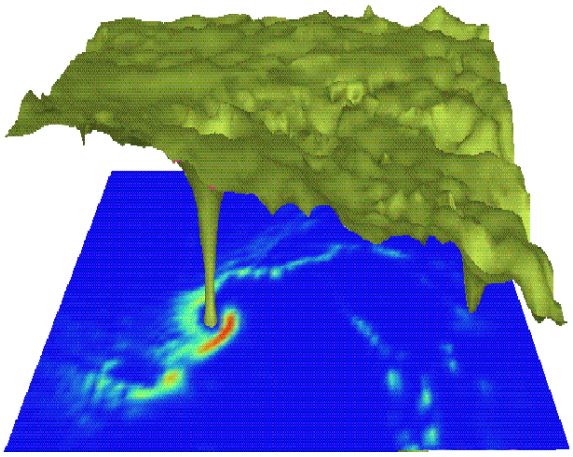

Fig. 7. Three-dimensional view of the simulated polar low of MRI-NHM valid at 1800 UTC 21 January 1997. The yellow-green color presents the isentropic surface of θ=271.5 K. The "warm core" structure near the polar low center is visualized by the funnel-like isentropic surface that almost reaches to the sea surface. The rainbow color shows the horizontal distribution of snow mixing ratio q_s near the sea surface, which corresponds well to the spiral-shaped cloud pattern and an "eye" structure.

(Fig. 6d). Thus, it is concluded in the "eye" region that the "warm core" structure in the potential temperature is mainly caused by the downward transport of the high potential temperature air, i.e., adiabatic warming associated with the downdraft when it is viewed in the temperature field.

Figure 7 shows a three-dimensional view of the simulated polar low based on the result of MRI-NHM valid at 1800 UTC 21 January 1997. The yellow-green color depicts the isentropic surface of θ=271.5 K. The "warm core" structure near the polar low center caused by adiabatic warming associated with the downdraft is clearly visualized by the funnel-like isentropic surface that almost reaches the sea surface. The horizontal distribution of the rainbow color shows the mixing ratio of snow q_s near the sea surface. The spiral-shaped cloud pattern and an "eye" structure as observed by satellite are clearly seen.

For tropical cyclones, Anthes (1982, p.30) pointed out that "the large temperature excess in the eye is due to adiabatic warming associated with subsidence. The downdraft in the eye region plays a particularly important role. It implies adiabatic warming and subsequently low central pressure". Yamasaki (1982, p.171) also indicated that the "warm core" near the typhoon "eye" was mainly caused by the downdraft. The present study shows that the formation mechanism of the "warm core" structure of the polar low is similar to that found in tropical cyclones.

3.4 *The CISK mechanism*

Anthes (1982, p.30) mentioned that an "eye" plays a fundamental role in producing the warm core, low central pressure, and strong winds associated with the hurricane. Furthermore, the lower pressure in the "eye" area accelerates the inflow of moist air, increases the release of latent heat, and has a positive feedback on the rest of the circulation. Grønås and Kvamstø (1995) also speculated that an "eye" was a sign of CISK taking place. As a clear "eye" was simulated successfully by using 5-km MRI-NHM in the present study, we will examine if the CISK mechanism is really working for the present polar low development.

Figure 8 shows the hourly vertical profiles of the area-mean condensational diabatic heating rate $d\overline{Q}/dt$, the vertical velocity $\overline{W}$, the divergence of the moisture flux $\overline{M} = \partial(uq_v)/\partial x + \partial(vq_v)/\partial y$, and circulation $\overline{C}$ from 1400 to 1900 UTC, where the area-mean is taken within a 50 km×50 km square area which is placed around the simulated surface polar low center*.

The diabatic heating rate (Fig. 8a) at the earlier stage was not very large. As the time elapsed, however, $d\overline{Q}/dt$ increased sharply from 0.8 K h^{-1} at 1400 UTC to 1.8 K h^{-1} at 1500 UTC. A large amount of latent heat was released during that period of time. At 1600 UTC, the diabatic heating rate at every level reached its peak. The maximum value appeared around the height 800–1800 m. At 1700 UTC, the magnitude of the diabatic heating decreased slightly, but still retained its relatively large value. It should be noted that during that period of time, the diabatic heating due to the latent heat release only occurred below 5000 m, and their maximum values appeared between 1000 and 2000 m. This clearly shows that the height of the latent heat release within the polar low is lower than that of the hurricane/typhoon.

The vertical distribution of $\overline{W}$, the area-mean vertical velocity (Fig. 8b), is quite similar to that of $d\overline{Q}/dt$, implying that the diabatic heating is nearly compensated by the adiabatic cooling in the central area of the polar low. The maximum area-mean updraft is located at around 1500 m with a value of 0.2–0.3 m s^{-1}.

Figure 8c shows the area-mean divergence of the moisture flux $\overline{M}$. It is seen that the moisture convergence (negative value) is confined below 1500 m, while weak divergence (positive value) exists above this height. At 1400 UTC, the convergence is weak with a maximum value of –0.25×10^{-6} kg kg^{-1} s^{-1} near the

*Similar calculations using different sizes of the square area are found to give similar results.

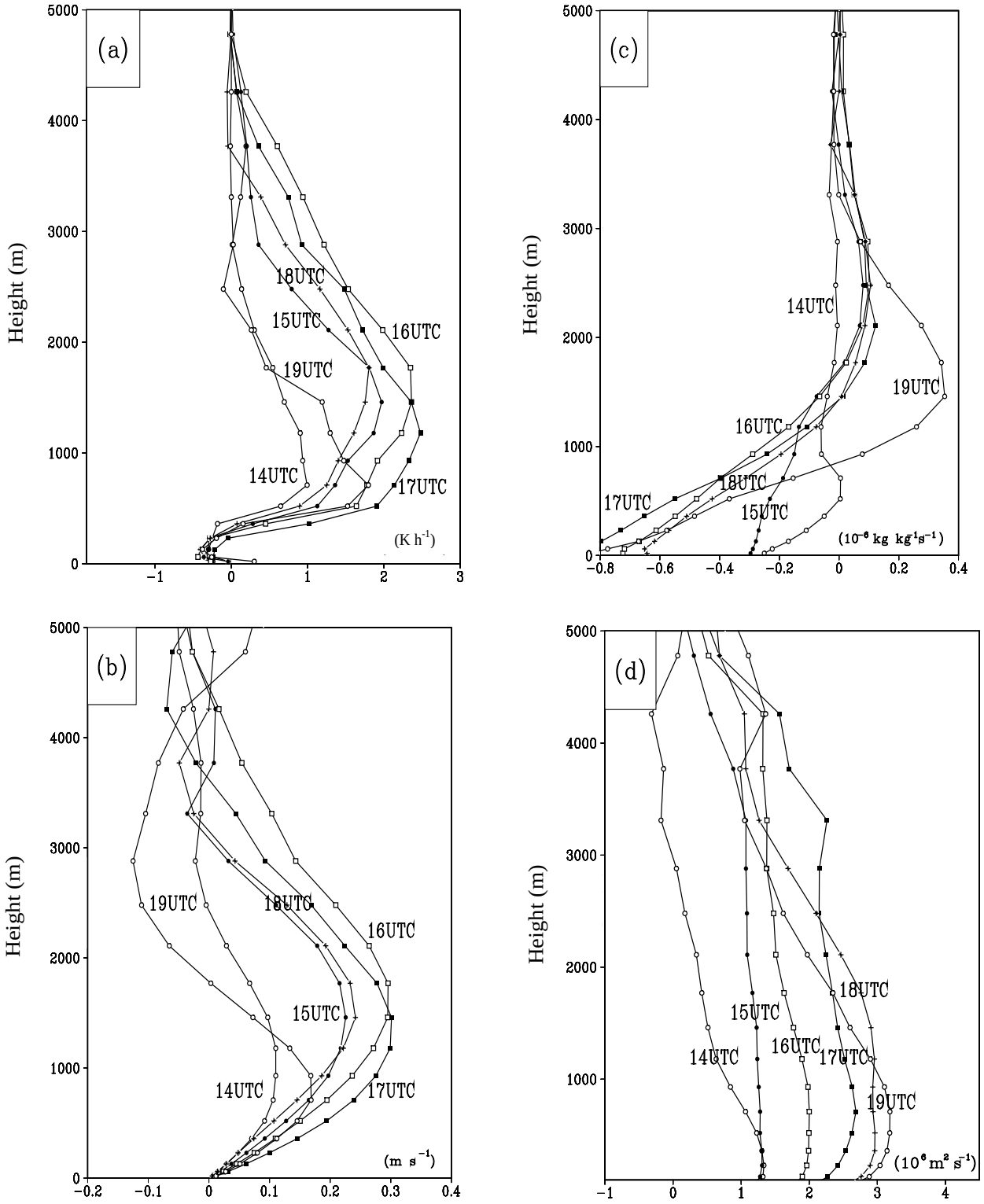

Fig. 8. (a) The area-mean condensational diabatic heating rate $d\overline{Q}/dt$ (in K h^{-1}) with respect to height. The calculations are shown for 1400, 1500, 1600, 1700, 1800, and 1900 UTC, respectively. (b) same as (a) but for area-mean vertical velocity $\overline{W}$ (m s^{-1}). (c) same as (a) but for the area-mean horizontal divergence of moisture flux $\overline{M}$ (in 10^{-6} kg kg^{-1} s^{-1}). (d) The area-mean circulation $\overline{C}$ (in 10^6 m^2 s^{-1}) with respect to height.

surface. It remains weak until 1500 UTC, but increases sharply to -0.80×10^{-6} kg kg^{-1} s^{-1} by 1600 UTC and maintains a similar magnitude later.

Figure 8d shows the area-mean circulation $\overline{C}$ calculated by a line integral along the four sides ofthe square area around the polar low. At 1400 UTC, the circulation $\overline{C}$ has the maximum value 1.4×10^{6} m^2 s^{-1} near the surface at the height of 250 m. It remains small near the surface until 1500 UTC. By 1700 UTC, the circulation has rapidly increased its value to 2.7×10^{6} m^2 s^{-1}. These changes in the circulation reflect the rapid increase of rotation of the polar low in association with the intensification of the vertical velocity. At 1800 and 1900 UTC, the circulation increased continuously, and the peak value appeared around 500–600 m.

Though the increases of $d\overline{Q}/dt$ and $\overline{W}$ start at 1500 UTC, those of $\overline{C}$ and $\overline{M}$ start one hour later. This appears to indicate that the frictional convergence in the boundary layer does not become effective until the vortex reaches certain strength. It is also noted that the circulation increases even after the diabatic heating $d\overline{Q}/dt$ and the vertical velocity $\overline{W}$ start to decrease after 1600 UTC. As far as the vertical velocity $\overline{W}$ causes an inflow of air having a larger circulation from the side boundaries, the area-mean circulation can increase with time.

In summary, the results presented in Fig. 8 show that the condensational heating, the vertical velocity, the convergence of the moisture flux, and the circulation averaged within a square area around the polar center formed a positive feedback loop during the development stage of the polar low. This loop is not inconsistent with the concept of the CISK mechanism (Ooyama, 1964; Charney and Eliassen, 1964).

4. Discussion and conclusion

Previous studies indicated that development of different polar low cases might be dominated by different mechanisms. Tsuboki and Wakahama (1992) indicated that baroclinic instability played a dominant role for the development of a polar low. Based on data analyses of the observations and the linear quasi-geostrophic instability analysis, they concluded that the mesoscale cyclones were generated as a result of baroclinic instability.

It should be pointed out that the horizontal scale of the polar lows in Tsuboki and Wakahama's study was approximately 500–700 km and was quite larger than the present case. The horizontal scale of the present polar low is only about 200 km, and is considerably smaller than Tsuboki and Wakahama's case. A comprehensive analysis of energy conversion (Fu, 1999) indicated that evidence for supporting the baroclinic development of the present polar low case was not sufficient, although we cannot deny its role in the development of the present polar low. The simulation by MRI-NHM suggested that the positive feedback loop among the condensational heating, vertical velocity, convergence of moisture convergence, and the area-mean circulation is not inconsistent with the CISK-like process.

Finally, we conclude the present study as follows. A remarkable polar low observed over the Sea of Japan on 21 January 1997 was successfully simulated by using a 5-km mesh MRI-NHM. The 24-h simulation by MRI-NHM reproduced the wrapping of the western part of an initial E–W oriented cloud band, the spiral-shaped pattern, and the "eye" structure of the vortex surprisingly well. The simulated polar low exhibited a large deviation from an axisymmetry. The wind speed associated with the polar low was much larger on the western side of the low center than on the eastern side. Accordingly, the surface heat flux was also much larger on the western side. The "eye" was occupied by warm dry air associated with a strong downdraft, and was almost free of cloud. The detailed thermodynamic budget analysis indicated that the "warm core" in "eye" region was mainly caused by the adiabatic warming associated with the downdraft. The relationship among the condensational diabatic heating, the vertical velocity, the convergence of the moisture flux, and the circulation averaged within a 50 km×50 km square area around the vortex center showed that they formed a positive feedback loop during the development stage of the polar low, and this loop is not inconsistent with the CISK concept.

Acknowledgments. The 5-km mesh simulation of MRI-NHM in the present study was finished in Japan with the help of Dr. Teruyuki Kato of the Meteorological Research Institute of Japan when the first author studied at the Ocean Research Institute, University of Japan. The first author would like to express his hearty thanks to Profs. Ryuji Kimura and Hiroshi Niino at the Dynamic Marine Meteorology Group, Ocean Research Institute, University of Tokyo for their suggestions, comments, and criticism. He is also very thankful to Mr. Takeuchi, Mr. Nishigata, and Mr. T. Yao of the Japan Meteorological Agency for providing data, and to Prof. Shang-Ping Xie for his helpful comments on the original manuscript. Thanks are also extended to staff and students at the Dynamic Marine Meteorology Group, Ocean Research Institute, University of Tokyo for their kind help.

The first author was partly supported by the Chinese Ministry of Education, and the Japanese Ministry

of Education, Science and Culture through their scholarship exchange programs, and the National Natural Science Foundation of China under the Grant Nos. 40275033 and 40240420564. This work was also supported by the State Key Laboratory of Atmospheric Boundary Layer Physics and Atmospheric Chemistry (LAPC) of the Institute of Atmospheric Physics of the Chinese Academy of Sciences under Grant No. LAPC-KF-2003-10.

REFERENCES

Anthes, R. A., 1982: Tropical cyclones: Their evolution, structure and effects. *Meteor. Monogr.*, **19**, Amer. Meteor. Soc., 208pp.

Charney, J. G., and A., Eliassen, 1964: On the growth of the hurricane depression. *J. Atmos. Sci.*, **21**, 68–75.

Fu Gang, 1999: An observational and numerical study on polar lows over, the Japan Sea. Ph. D dissertation, University of Tokyo, 109pp.

Fu Gang, 2001: *Polar Lows: Intense Cyclones in Winter*. China Meteorological Press, Beijing, 218pp.

Fu, G., H. Niino, R. Kimura, and T. Kato, 2004: Multiple Polar Mesocyclones over the Japan Sea on 11 February 1977. *Mon. Wea. Rev.*, **132**, 793–814.

Gal-Chen, T., and R. C. Somerville, 1975: On the use of a coordinate transformation for the solution of the Navier-Stokes equations. *J. Comp. Phys.*, **17**, 209–228.

Grønås, S., and N. G. Kvamstø, 1995: Numerical simulations of the synoptic conditions and development of arctic outbreak polar lows. *Tellus*, **47A**, 797–814.

Harley, D. G., 1960: Frontal contour analysis of a "polar low" . *Meteor. Mag.*, **89**, 146–147.

Ikawa, M., and K. Saito, 1991: Description of a nonhydrostatic model developed at the Forecast Research Department of the MRI. *Tech. Rep. of the MRI*, **28**.

Kato, T., 1995: A box-Lagrangian rain-drop scheme. *J. Meteor. Soc. Japan*, **73**, 241–245.

Kato, T., 1996: Hydrostatic and non-hydrostatic simulations of the 6 August 1993 Kagoshima torrential rain. *J. Meteor. Soc. Japan*, **74**, 355–363.

Kondo, J., 1975: Air-sea bulk transfer coefficients in diabatic conditions. *Bound.-Layer Meteor.*, **9**, 91–112.

Lee, T. Y., Y. Y. Park, and Y. L. Lin, 1998: A numerical modeling study of mesoscale cyclogenesis to the east of Korean Peninsula. *Mon. Wea. Rev.*, **126**, 2305–2329.

Mansfield, D. A., 1974: Polar lows: The development of baroclinic disturbances in cold air outbreaks. *Quart. J. Roy. Meteor. Soc.*, **100**, 541–554.

Nakamura, M., 1995: Verification of the new JSM. *Text for the numerical prediction*, Forecast Department of the Japan Meteorology Agency, **25**, 10–38.

Ninomiya, K., 1989: Polar/comma-cloud lows over the Japan Japan Sea and the northwestern Pacific in winter. *J. Meteor. Soc. Japan*, **67**, 83–97.

Ooyama, K., 1964: A dynamical model for the study of tropical cyclone development. *Geophys. Intern.*, **4**, 187-198.

Rasmussen, E., 1979: The polar low as an extratropical CISK-disturbance. *Quart. J. Roy. Meteor. Soc.*, **105**, 531–549.

Saito, K., 1993: A numerical study of the local downslope wind "Yamaji-kase" in Japan. Part 2: Non-linear aspect of the 3-D flow over a mountain range with a col. *J. Meteor. Soc. Japan*, **71**, 69–91.

Saito, K., 1994: A numerical study of the local downslope wind "Yamaji-kase" in Japan. Part 3: Numerical simulation of the 1991 September wind-storm with a non-hydrostatic multi-nested model. *J. Meteor. Soc. Japan*, **72**, 301–329.

Saito, K., 1997: Semi-implicit fully compressible version of the MRI mesoscale non-hydrostatic model—Forecast experiment of the 6 August 1993 Kagoshima Torrential rain. *Geophys. Mag.*, **2**, 109–137.

Saito, K., 1998: On the MRI mesoscale nonhydrostatic model. Tech. Rep. for the annual meeting of the JMA for the improvement of forecasting techniques, 19-20 February 1998, Tokyo, Japan, MRI, 39–58. (in Japanese)

Saito, K., and T. Kato, 1996: On the modification of the MRI nonhydrostatic nesting model. *Tenki*, **43**, 369–382. (in Japanese)

Shapiro, M. A., L. S. Fedor, and T. Hampel, 1987: Research aircraft measurements of a polar low over the Norwegian Sea. *Tellus*, **39A**, 272–306.

Sommeria, G., 1976: Three-dimensional simulation of turbulent processes in an undisturbed trade wind boundary layer. *J. Atmos. Sci.*, **33**, 216–241.

Tsuboki, K., and G. Wakahama, 1992: Mesoscale cyclogenesis in winter monsoon air streams: Quasi-geostrophic baroclinic instability as a mechanism of the cyclogenesis off the west coast of Hokkaido Island, Japan. *J. Meteor. Soc. Japan*, **70**, 77–93.

Yamasaki, M., 1982: *Typhoon*, Tokyo-do Press, 206pp. (in Japanese)

Yanase, W., H. Niino, and K. Saito, 2002: High-resolution numerical simulation of a polar low. *Geophys. Res. Lett.*, 10.1029/2002GL014736.